ARTICLE

OPEN

Check for updates

A high-resolution time-variable terrestrial gravity field model of continental North China

Jiancheng Han [1,2], Shi Chen [1,2 ✉], Hongyan Lu[1,2], Lulu Jia[1,2], Linhai Wang [1,2], Weimin Xu[1,2], Huai Zhang[3] & Heping Sun [4]

Given the spatial resolution of ~300 km in Gravity Recovery and Climate Experiment (GRACE) measurements, accurately quantifying mass variations at smaller scales proves challenging. Here, we present a high-resolution time-variable gravity field model of continental North China. This model, denoted as IGP-NorthChina2022TG, contains 15 gravity field solutions determined using an innovative approach that relies on terrestrial gravity measurements and Slepian basis functions. IGP-NorthChina2022TG provides degree 150 gravity changes (spatial resolution of ~120 km) on a semi-annual basis from September 2009 to September 2016, in contrast to the monthly degree 60 GRACE solutions. Despite their different temporal resolutions, the good agreement between GRACE and the ground-based results up to degree 60 confirms the robustness and reliability of the proposed method and favors the combination of these two types of measurements. The gravity changes with much finer spatial resolution from IGP-NorthChina2022TG could complement GRACE solutions for sub-regional scale investigations in North China.

[1] Beijing Baijiatuan Earth Sciences National Observation and Research Station, Beijing 100095, China. [2] Institute of Geophysics, China Earthquake Administration, Beijing 100081, China. [3] Key Laboratory of Computational Geodynamics, University of Chinese Academy of Sciences, Beijing 100049, China. [4] State Key Laboratory of Geodesy and Earth's Dynamics, Innovation Academy for Precision Measurement Science and Technology, Chinese Academy of Sciences, Wuhan 430077, China. ✉email: chenshi@cea-igp.ac.cn

The time-variable gravity field, which reflects mass variations within the Earth system, is one of the keys to understanding the changing Earth. The mass variations are caused by the transport and redistribution of mass at the Earth's surface and in its interior (crust, mantle, and core). Since its launch in 2002, the Gravity Recovery And Climate Experiment (GRACE) and its follow-on mission have revolutionized how we observe and understand global mass variations by measuring the time-variable gravity field[1].

North China is a region with well-developed active faults (Fig. 1a) and a high seismic hazard level. North China is also a substantial industrial base and grain-producing area, featuring a dense population and high water demand. Because of insufficient precipitation, groundwater has become the primary source of intensive industrial, agricultural, and domestic water use in North China and has been overexploited since the 1970s[2,3]. Long-term groundwater overexploitation has caused the development of numerous cones of depression in the North China Plain (NCP; Fig. 1b), resulting in severe land subsidence (Fig. 1a) that affects sustainable economic and social development[4–6]. Furthermore, overexploitation of groundwater in North China unloads the lithosphere and contributes to the deformation of bedrock, which may trigger the occurrence of earthquakes in this region[7,8]. Time-variable gravity measurements from GRACE not only offer an independent tool to monitor and analyze groundwater storage (GWS) depletion in North China[3,9–17], but also facilitate estimates of the uplift rate (at the sub-millimeter per year level) in the same region[7,8,18].

Despite many successful applications in North China, accurately quantifying mass variations at small scales is still challenging due to the coarse spatial resolution (~300 km[3,19]) of GRACE measurements. Moreover, for popular GRACE products in terms of spherical harmonics (SH), an additional postprocessing step such as decorrelation and spatial smoothing[20,21] is necessary to reduce the correlated and high degree errors. However, postprocessing is accompanied by signal attenuation and distortion[3,22,23]. As alternatives to SH products, the mascon GRACE products provide grid results with improved resolutions that can be used directly without postprocessing[24–27]. However, previous studies have pointed out that the spatial resolution of the mascon products is still relatively low, ranging from 200 km to 300 km[28,29].

Unlike the high-orbit GRACE observations, the terrestrial time-variable gravity measurements are collected at the Earth's surface by regularly observing all stations in a network[30,31]. For example, the field observations for the gravity network in North China (GNNC) are performed semiannually[32]. As part of the continental-scale gravity network established across the Chinese mainland, GNNC consists of 18 absolute-gravity stations and approximately 500 relative-gravity stations[32]. The distance between adjacent stations in GNNC ranges from several hundred meters to approximately 200 km. Consequently, gravity measurements from GNNC can provide information at a higher spatial resolution than the GRACE results. Moreover, terrestrial measurements are more accurate at short wavelengths due to the inherent signal attenuation with altitude of the gravity field[33].

In this study, we focus on developing a high-resolution time-variable gravity field model in North China solely from terrestrial measurements. The development includes 15 repeated survey campaign measurements from GNNC between September 2009
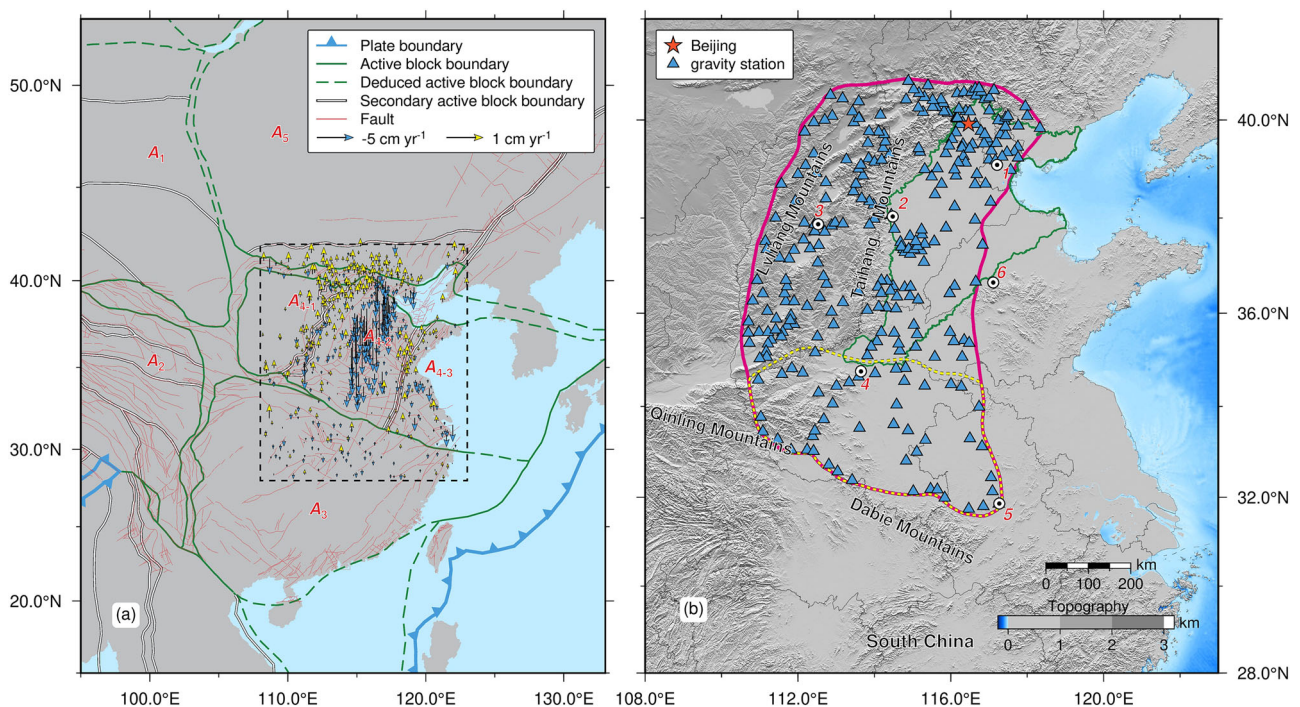

Fig. 1 Tectonic setting and severe subsidence in North China. a Green lines delineate the boundaries of the active blocks: Xiyu (A_1), Tibetan Plateau (A_2), South China (A_3), North China (A_4), and Northeastern Asia (A_5). White lines delineate the boundaries of the secondary active blocks: Ordos (A_{4-1}), North China Plain (A_{4-2}), and Eastern Shandong-Yellow Sea (A_{4-3}). All block data are taken from Zhang et al.[75]. Thin red lines show the active faults[76]. The GPS-derived vertical displacement rates in North China[8,17] are indicated by yellow and blue arrows, where negative rates represent subsidence. **b** Blue triangles show the locations of the repeated survey gravity stations. Magenta, green, black, and yellow dashed lines denote the boundaries of the region of interest, the North China Plain (NCP), the provincial borders, and a region with sparse stations, respectively. Number 1 denotes the Tianjin Municipality, and numbers 2 to 6 denote Shijiazhuang (capital city of Hebei Province), Taiyuan (capital city of Shanxi Province), Zhengzhou (capital city of Henan Province), Hefei (capital city of Anhui Province), and Jinan (capital city of Shandong Province), respectively. The shaded topography in the background is from SRTM15+[77].

and September 2016 (see the Methods section, dataset subsection). Here, we present the derived time-variable gravity field model in North China with 15 solutions up to degree 150 (d150), as well as a tailored method for recovering regional gravity field based on Slepian basis functions[34–36] and terrestrial measurements (see Methods, Supplementary Methods 1 and 2). In addition, we show that the derived d150 solutions provide gravity changes with finer spatial resolution and stronger signal strength compared with GRACE-derived results for investigations at subregional scales.

Results and discussion

Overview of the modeling methods. We propose a tailored method for regional gravity field modeling using Slepian basis functions, which is comprehensively described in the Methods section, Supplementary Methods 1 and 2. This method consists of two key stages: model selection and the mitigation of broadband leakage. A brief overview of this method is outlined below. In the first stage, the maximum spherical expansion degree N and the optimal truncation level J_{opt} are determined using a two-step procedure. Within a given region, a subset of the Slepian basis functions tends to be well-concentrated, while the others are not. Consequently, it is reasonable to use the subset of well-concentrated Slepian basis functions to optimally model the signal confined to the specific region and omit the rest. The number of this subset of Slepian basis functions is termed the optimal truncation level and denoted by J_{opt}. Once these parameters (N and J_{opt}) are determined, their corresponding model is selected as the optimal one. In the second stage, the broadband leakage is mitigated using an iterative strategy based on Gaussian spatial averaging. This is an important issue in Slepian analyses that few studies have addressed. Broadband leakage arises from the discrepancy between the maximum expansion degree N and that contained in the input signals (which is infinity for in situ measurements). When modeling a degree N field, the high degree ($>N$) components in the input signal will affect the estimation of the coefficients at lower degrees ($\leq N$). As detailed in the Methods section, Supplementary Methods 1 and 2, the proposed strategy effectively mitigates the broadband leakage.

Comparisons with GRACE-derived gravity changes. Before moving on to the d150 gravity field recovery in North China, we validated the proposed method (see Methods) by recovering a series of degree 60 (d60) fields and comparing them with the GRACE-derived results. Using terrestrial gravity measurements, we first set the optimal truncation level J_{opt} and the Gaussian spatial averaging radius r [km] for the d60 field recovery to 3 and 512, respectively. A series of 15 d60 gravity solutions were obtained using these parameters and the terrestrial gravity measurements (see Supplementary Note 1 and Supplementary Figs. 7 and 8). We then estimated the rates of the d60 gravity changes dg_{TG}^{d60}/dt (where TG indicates terrestrial gravity) in North China by least-squares fitting a linear model to the time series at each grid node of the 15 d60 solutions. The seasonal variations are not estimated due to the semi-annual temporal resolution of TG measurements (see Datasets). Figure 2a shows the derived linear rates and reveals an overall increasing pattern over the entire region of interest, with a dominant gravity increase centering around the city of Shijiazhuang in the northern part of the region of interest. Next, we examined the vertical displacements in the region of interest. The GRACE results are derived at the space-fixed points[37–39], while the terrestrial measurements are derived on the Earth's surface, which is associated with vertical displacements (either uplift or subsidence). For example, the NCP (see Fig. 1b and Supplementary Fig. 9b) in the region of interest

has suffered from severe land subsidence during the past several decades[5,6,13,17]. Therefore, we need to remove the gravity effects induced by the vertical displacements in the region of interest prior to the comparison. It is accomplished by incorporating the GPS vertical displacement measurements (Supplementary Note 2). We recovered a d60 field, dh_{GPS}^{d60}/dt (Supplementary Fig. 9c), from these GPS vertical displacement rates using the same above-determined J_{opt} and r parameters.

We then accounted for the gravity effects induced by vertical displacements using different gravity gradient γ_g in North China (see Methods), namely the free-air gradient ($\gamma_g = -3.086$ μGal cm^{-1}), the Bouguer gradient ($\gamma_g = -1.967$ μGal cm^{-1}) and the Bouguer-corrected free-air gradient (BCFAG$_{spherical}$) of a spherical source ($\gamma_g = -3.086 + 4\pi G\rho_0/3$ μGal cm^{-1})[40,41], where G is the gravitational constant and ρ_0 is the density of the source. The BCFAG$_{spherical}$ represents the gravity changes associated with a change in elevation, taking into account the mass accompanying the deformation[33]. Assuming a spherical magma source, the BCFAG$_{spherical}$ is widely adopted in dealing with gravity changes in volcanic systems[33,40,41]. Since the land subsidence in the NCP has a strong relationship with groundwater overexploitation[5], we assume a spherical source of groundwater by analogy with the volcanic case when applying the BCFAG$_{spherical}$ correction. With groundwater density of 1000 kg m^{-3}, the BCFAG$_{spherical}$ results in $\gamma_g = -2.806$ μGal cm^{-1}.

The gravity effects induced by vertical displacements $\gamma_g dh_{GPS}^{d60}/dt$ with γ_g as the free-air and Bouguer gradients (see Eq. 4 in Methods) are shown in Supplementary Figs. 12a and 12d, respectively. The gravity effects $\gamma_g dh_{GPS}^{d60}/dt$ with γ_g as the BCFAG$_{spherical}$ gradient are shown in Fig. 2b. After accounting for the vertical displacement effects, the residual gravity rate dg_{res}^{d60}/dt (see Eq. 4) in Fig. 2c is comparable to the GRACE-derived gravity rate.

As an independent estimation of the gravity changes, three sets of GRACE-derived gravity rates (see Supplementary Note 3 for details) over the region of interest are presented in Fig. 2d–f. These d60 rates using GRACE data all show a consistent pattern of gravity decreases over the region of interest, with the most notable decrease close to the border of three provinces (Hebei, Henan, and Shandong). The rates with the least attenuated signal strength among the GRACE-derived d60 rates are those derived using Slepian functions (Fig. 2d), which do not require smoothing or filtering. The d60 results obtained using the DDK (Fig. 2e) and Gaussian smoothing filters (Fig. 2f) further attenuate the signal power. For example, the mean d60 rates in the NCP from 2009 to 2016 are -1.27 (Slepian-derived GRACE, Fig. 2d), -1.00 (DDK-derived GRACE, Fig. 2e), and -0.99 μGal yr^{-1} (Gaussian-derived GRACE, Fig. 2f). Hence, we use the Slepian-derived GRACE results in Fig. 2d as a benchmark in comparison with the d60 rates derived using terrestrial measurements. Note that parts of the NCP are outside the region of interest (Fig. 1b). Hereafter, we refer to the majority of the NCP, which lies inside the region of interest, as NCP for brevity.

Using different gravity gradients (Eq. 4), we derived three sets of d60 gravity residual rates dg_{res}^{d60}/dt based on the terrestrial gravity and GPS measurements in North China, as shown in Supplementary Figs. 12b, 12e and 12h (Supplementary Note 4), respectively. The differences between terrestrial- and GRACE-derived gravity rates (Fig. 2d) in North China are shown in Fig. 3 and Supplementary Figs. 12c, 12f and 12i. In the region of interest, the correlation coefficient between dg_{res}^{d60}/dt derived using free-air gradient and GRACE rates has the largest value (0.898), followed by that between dg_{res}^{d60}/dt using the
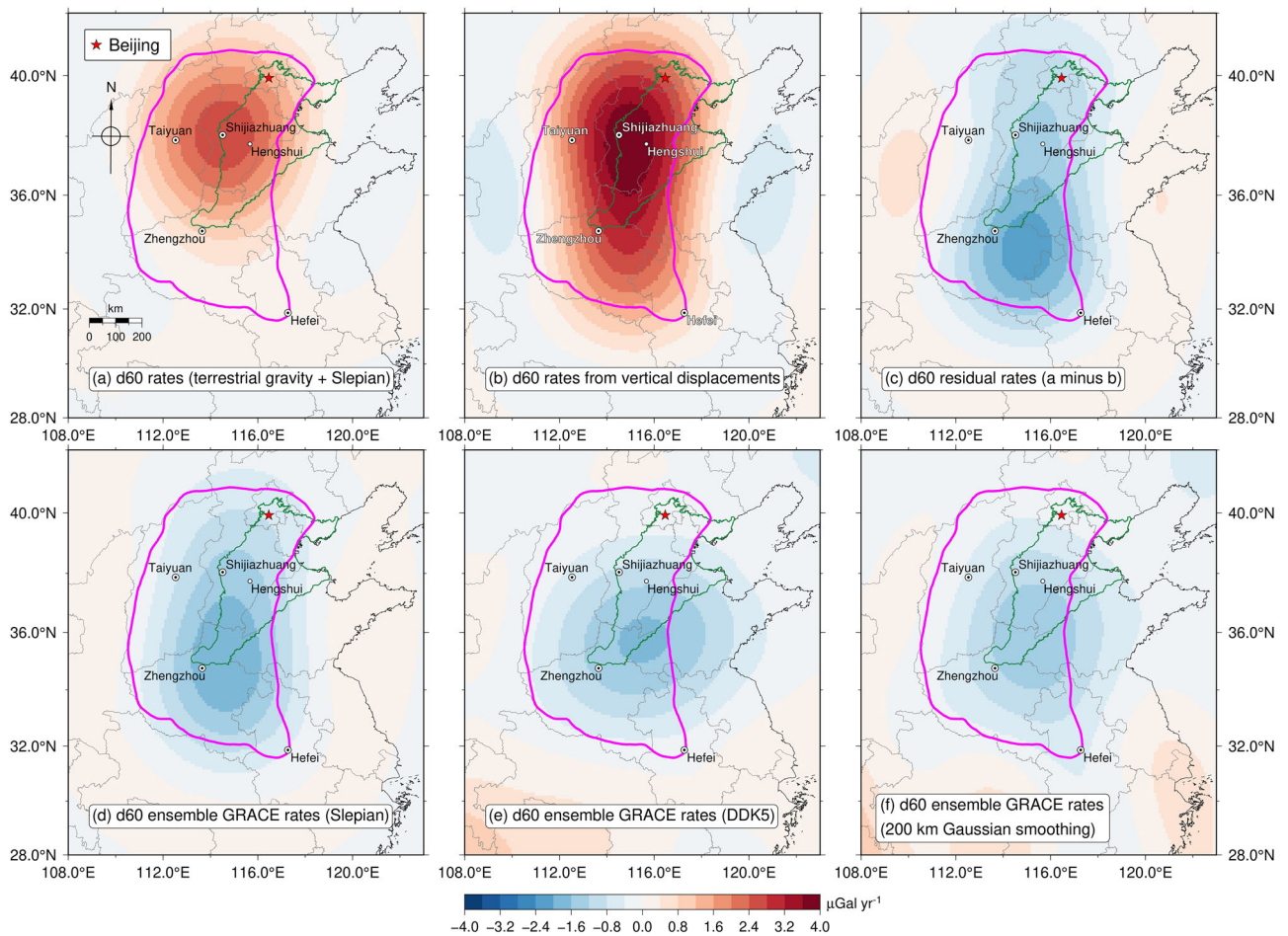
Fig. 2 Comparison of terrestrial- and GRACE-derived gravity rates in North China. a Rates of the degree 60 gravity changes derived using Slepian functions and terrestrial gravity measurements; **b** rates of the gravity changes induced by vertical displacement up to degree 60; **c** residual rates (subtracting panel **b** from panel **a**); **d** ensemble rates of Slepian-derived GRACE gravity changes; **e** ensemble rates of DDK5 (denoising and decorrelation kernel version 5)-derived GRACE gravity changes; and **f** ensemble rates of Gaussian smoothing-derived GRACE gravity changes. The magenta line denotes the boundary of the region of interest. The green line shows the boundary of the NCP, the black line indicates the land-ocean boundary and the gray lines show the provincial borders.
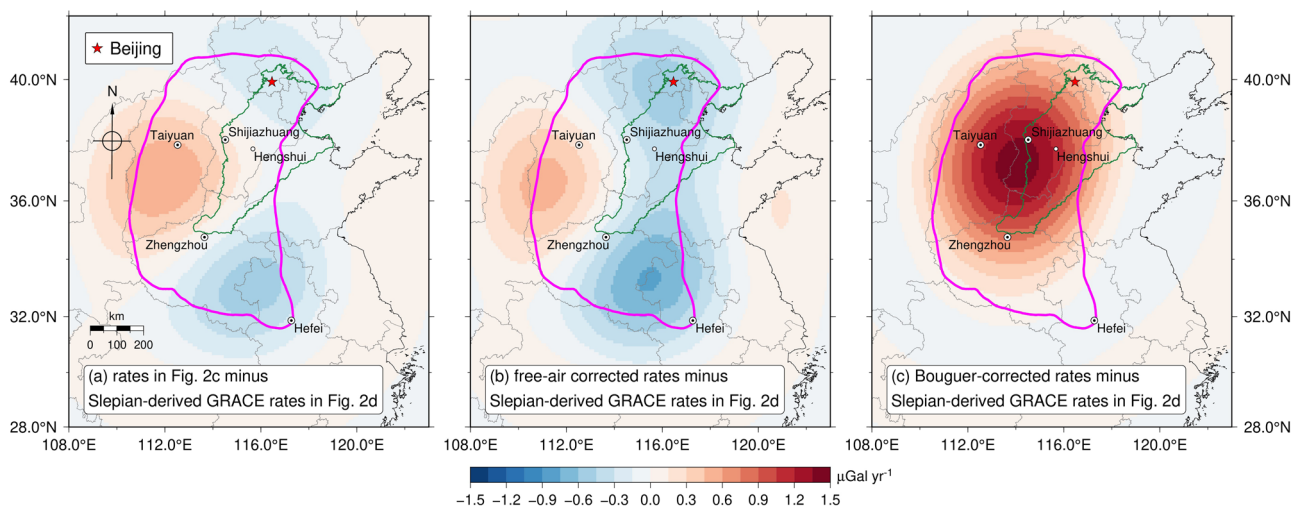

Fig. 3 Differences between terrestrial- and GRACE-derived gravity rates in North China. These differences are calculated by subtracting GRACE-derived rates in Fig. 2d from terrestrial residual rates corrected by **a** Bouguer-corrected free-air gradient of a spherical source; **b** free-air gradient; and **c** Bouguer gradient. The magenta lines denote the boundary of the region of interest, the green lines show the boundary of the NCP, the black lines indicate the land-ocean boundary, and the gray lines show the provincial borders. Note that the color bar is different from that in Fig. 2.

BCFAG$_{spherical}$ and GRACE rates (0.878), and the correlation coefficient between dg_{res}^{d60}/dt derived using the Bouguer gradient and GRACE rates has the smallest value (0.671). These correlation coefficients and the differences in Fig. 3 indicate that the Bouguer gradient is inadequate to account for the gravity effects induced by vertical displacements in North China, especially in the NCP. Over the region of interest, the difference in the free-air case (Fig. 3a) and that in the BCFAG$_{spherical}$ case (Fig. 3b) show negative-positive-negative spatial patterns from north to south. In comparison, the difference in the Bouguer case (Fig. 3c) shows a prominent positive pattern. Moreover, we examined the mean and root mean square for the differences of the three cases in the NCP. The mean and root mean square are −0.040 and 0.147 µGal yr^{-1} for the BCFAG$_{spherical}$ case, −0.365 and 0.379 µGal yr^{-1} for the free-air case, and 0.909 and 0.962 µGal yr^{-1} for Bouguer case. These analyses show that the BCFAG$_{spherical}$ performs the best in the region of interest among the three vertical gravity gradients.

This good agreement between the satellite- and ground-based results confirms the robustness and reliability of the model selection and leakage mitigation strategies (see Methods). Moreover, this comparison implies that ground-based gravity field solutions can be applied to validate satellite-based solutions. In addition, the signals derived using Slepian functions (Fig. 2c and d) are well concentrated in the region of interest. Those derived using the DDK and Gaussian smoothing filters are smeared out, inducing spatial leakage (evident at the land-ocean boundary). This contrast further highlights the benefits of Slepian functions for regional analyses.

Degree 150 gravity field solutions. Based on the proposed methods, we recovered a series of 15 solutions up to degree 150 (d150) solely from repeated campaign measurements at the 287 gravity stations, covering the period from September 2009 to September 2016 (Fig. 4a–o). The spatial resolution is ~120 km (half-wavelength). We call these solutions IGP-North-China2022TG, where TG indicates that each solution was derived solely from terrestrial gravity measurements.

Next, we estimated the linear rates from September 2009 to September 2016 for the degree 150 gravity changes, g_{TG}^{d150}/dt, in North China from IGP-NorthChina2022TG (Fig. 4) using least-squares fitting, as we did for g_{TG}^{d60}/dt. The derived rates, g_{TG}^{d150}/dt (Fig. 5a), show much finer spatial resolution and stronger signal strength compared with the rates from GRACE, revealing a decreasing–increasing–decreasing pattern from north to south over the region of interest. The first decreasing pattern is to the northwest of Beijing, with a negative peak reaching approximately −4 µGal yr^{-1}. Then, there is an increasing pattern over the middle part of the region of interest, including the majority of Shanxi Province, the southern part of Hebei Province, the western part of Shandong Province, and the northern part of Henan Province (see Fig. 1b for the locations of these provinces). The region with the most notable gravity increase (approximately 10 µGal yr^{-1}) is located around Hengshui, close to the border of the Hebei and Shandong provinces. This finding is similar to previous terrestrial gravity measurement studies, e.g., results from Shen et al.[42] from 2009 to 2013 and Hao et al.[43] from 2010 to 2014. As part of the NCP, this region also suffers from groundwater depletion and severe land subsidence[6,8,44,45]. Finally, there is an elongated, northwest–southeast-oriented, decreasing pattern over the southern part of the region of interest with two peaks (approximately −5 µGal yr^{-1}). One peak is just south of Zhengzhou in Henan Province, while the other is near Hefei in Anhui Province.

Both terrestrial and GRACE measurements capture integrated gravity changes originating from geophysical phenomena occurring at the surface and inside the Earth. Hence, the degree 150 gravity rate, dg_{TG}^{d150}/dt, is also an integration representing the mass changes from those phenomena. To help identify the gravity changes beneath the Earth's surface, we further removed gravity rates induced by vertical displacements and hydrological signals from the integrated rate, dg_{TG}^{d150}/dt. We first converted the d150 GPS vertical displacement rate, dh_{GPS}^{d150}/dt (Supplementary Fig. 9d), into gravity changes using the BCFAG$_{spherical}$ gradient (see Methods); the result is shown in Fig. 5b. Then, we used output from the WaterGAP Global Hydrology Model (WGHM) 2.2d[46,47] for the same months as the terrestrial gravity measurements to estimate the gravity effects induced by hydrological signals. The WGHM output includes changes in canopy storage, soil moisture storage, water-equivalent snow storage, and surface water storage (i.e., lakes, reservoirs, rivers, and wetlands). The sum of these storage changes in each month is first converted to gravity changes, from which we then estimate the rates of the hydrological signals, dg_{Hydro}^{d150}/dt. As shown in Fig. 5c, the variations in the derived dg_{Hydro}^{d150}/dt from WGHM 2.2d are much smaller than those in the gravity rate, dg_{TG}^{d150}/dt. For example, the mean dg_{Hydro}^{d150}/dt (−0.05 µGal yr^{-1}) only accounts for ~5% of the mean dg_{TG}^{d150}/dt over the region of interest (0.93 µGal yr^{-1}). We estimated two sets of degree 150 residual rates, g_{res}^{d150}/dt (see Eq. 4 in Methods), from September 2009 to September 2016 in North China. The first set (Fig. 5d) was derived by removing the linear rates induced by vertical displacements from the gravity rates dg_{TG}^{d150}/dt (Fig. 5a). The BCFAG$_{spherical}$ gradient was adopted in this procedure. The second set (Fig. 5e) was derived by further removing the hydrological rates dg_{Hydro}^{d150}/dt from the results in Fig. 5d. The first set of g_{res}^{d150}/dt could be directly compared with the GRACE-derived rates in Fig. 2d, since both results are based on observations and not corrected for hydrological contributions. The second set of g_{res}^{d150}/dt aims to isolate the effects primarily caused by GWS changes and tectonics. Note that any uncertainty of the adopted model for estimating the hydrological contributions will contribute to the uncertainty of the d150 residual rates. Here, the second set of g_{res}^{d150}/dt is affected by the uncertainty and limitation of the WGHM-based water storage changes in canopy, soil, snow, lakes, reservoirs, rivers, and wetlands. As we show later, WGHM 2.2d does not include all large reservoirs in North China in its estimation of surface water storage (Supplementary Fig. 14c). Previous study also shows that the WGHM-derived interannual rates are with large uncertainty[48].

Figure 5d, e show similar spatial patterns and roughly reveal a decreasing–increasing–decreasing pattern from north to south over the region of interest. A decreasing pattern is concentrated over the NCP with two peaks, with one peak (approximately −6 µGal yr^{-1}) around Beijing and the other (approximately −4 µGal yr^{-1}) around Hengshui. This pattern highlights a sub-regional difference in the decrease in the NCP, indicating that the decrease is faster in the eastern regions than in the piedmont regions. An increasing pattern occurs over the majority of Shanxi Province, with its peak (approximately 4 µGal yr^{-1}) close to the border between Shanxi and Henan provinces. This positive rate is clearly separated from the negative rate over the NCP along the Taihang Mountains (see Fig. 1b). A decreasing pattern with northwest-southeast orientation occurs over the southern part of the region of interest afterward. This pattern is similar to the negative pattern of the d150 gravity rates, dg_{TG}^{d150}/dt, in the same region but with a slightly stronger signal strength (negative peak value of
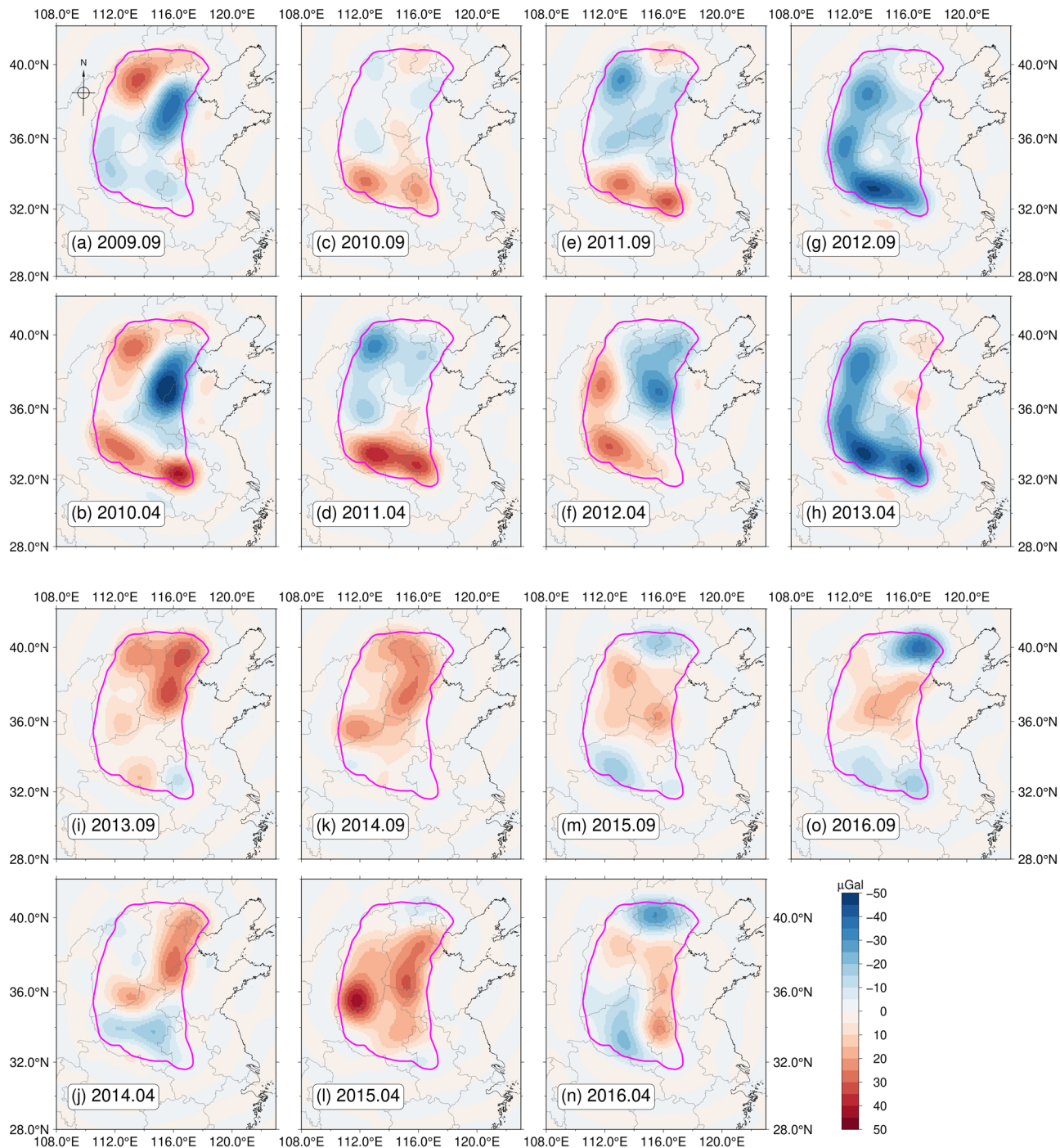
Fig. 4 The derived time-variable gravity field model (degree 150) in North China. Spatial pattern of the degree 150 solutions in **a** September 2009; **b** April 2010; **c** September 2010; **d** April 2011; **e** September 2011; **f** April 2012; **g** September 2012; **h** April 2013; **i** September 2013; **j** April 2014; **k** September 2014; **l** April 2015; **m** September 2015; **n** April 2016; and **o** September 2016. The mean of all 15 solutions is removed from each solution. This model is called IGP-NorthChina2022TG (where TG indicates terrestrial gravity) and has a temporal coverage from September 2009 to September 2016 on a semi-annual basis. The magenta line denotes the boundary of the region of interest, the black line indicates the land-ocean boundary, and the gray lines show the provincial borders.

approximately −6 μGal yr⁻¹) and a negative peak in Anhui Province moving northward.

We then compared the first set of d150 residual rates (Fig. 5d) with the d60 rates from GRACE (Fig. 2d). First, the d150 rates in Fig. 5d show a larger amplitude. For instance, the mean gravity rate in the North China Plain in Fig. 5d is −2.18 μGal yr⁻¹ (with a root mean square of 2.74 μGal yr⁻¹), nearly two times as large as the estimate of GRACE (−1.27 μGal yr⁻¹ in Fig. 2d). Second, the

d150 rates reveal more spatial details in North China. In principle, the d60 GRACE rates capture an overall decreasing trend in the region of interest. After removing these d60 rates from the first set of d150 rates, we obtained the degree 61 to 150 spherical harmonic components of gravity rates from September 2009 to September 2016 in North China. Prominent variations are visible to the northwest of Beijing (decreasing pattern), the south of Shanxi Province (increasing pattern) and the south of
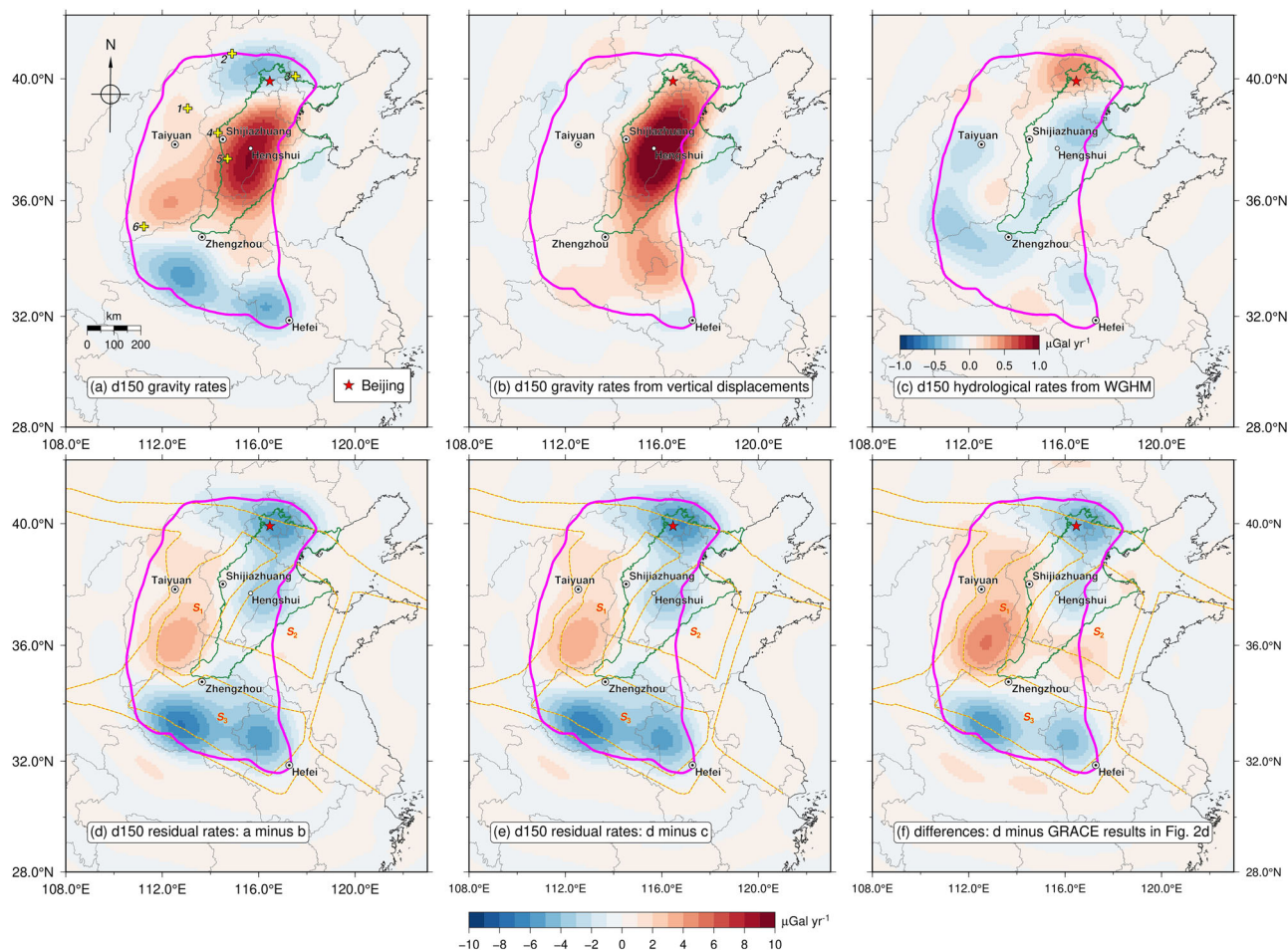
Fig. 5 Comparison of d150 gravity rates. a Gravity rates from the IGP-NorthChina2022TG degree 150 model (September 2009–September 2016), yellow crosses denoting the locations of the absolute gravity (AG) stations; **b** gravity rates induced by vertical displacement up to degree 150; **c** rates of hydrological effects from the WaterGAP Global Hydrology Model (WGHM) up to degree 150; **d** rates of the degree 150 residual gravity changes derived by subtracting panel **b** from panel **a**; **e** rates of the degree 150 residual gravity changes derived by subtracting panel **c** from panel **d**; and **f** difference between panel **d** and those in Fig. 2d. The yellow-red dashed line denotes the boundaries of the active blocks[78], with S_1 denoting the Taihangshan sub-block, S_2 denoting the Hebei-Shandong sub-block, and S_3 denoting the Henan-Huai sub-block. S_1, S_2, and S_3 belong to the NCP block (A_{4-2} in Fig. 1a). The magenta lines denote the boundary of the region of interest, the green lines show the boundary of the NCP, the black lines indicate the land-ocean boundary, and the gray lines show the provincial borders. Note that the color bar is different in panel **c**.

Henan Province and the northwest of Anhui Province (decreasing pattern) in the region of interest in Fig. 5f; however, these variations are not captured by GRACE.

Relationship between the GWS-induced gravity rates and the estimated d150 residual rates. We collected GWS statistics from the annual Water Resources Bulletins (WRB) from two municipalities (Beijing and Tianjin) and five provinces (Hebei, Henan, Shandong, Shanxi, and Anhui). For the WRB of each province, the GWS statistics are given city by city. All the GWS data provided in the WRB are volumes (units in 10^8 m^3). The GWS statistics for Beijing, Tianjin, Hebei, Henan, and Shandong cover the years from 2009 to 2016, the same as our study period. However, the available GWS statistics for Shanxi and Anhui do not completely cover the study period, with data in Shanxi from 2011 to 2016 and data in Anhui from 2009 to 2013 (with missing data in 2010). Figure 6a shows the rates of the GWS volume changes estimated from these official statistics for each city in the region of interest. After dividing the area for each city, we converted the rates of the volume changes into rates of equivalent water height changes; the result is shown in Fig. 6b. These water

height change rates are then converted to d150 gravity changes using Slepian functions (see Supplementary Methods 1 and 2 for details), as shown in Fig. 6c.

The WRB-based equivalent water height and gravity rates (Fig. 6b, c) highlight the depletion of GWS in the NCP and Henan Province, as well as the increase in GWS in Shanxi Province and part of Henan Province. It is worthwhile to note that possible GWS changes in deep aquifers are not included in Fig. 6b, c.

The WRB-based d150 rates indicate that (1) the most apparent depletion of GWS in the NCP occurred in the eastern regions from 2009 to 2016, while the piedmont regions in the NCP experienced a GWS increase during the same period; (2) two NCP regions show similar depletion rates, one occurring around Beijing and the other occurring to the south of Hengshui. The majority of Henan Province also experienced GWS depletion, with the maximum depletion occurring in Luoyang and Pingdingshan; (3) GWS increases occurred throughout the majority of Shanxi Province, with the maximum increase covering the cities of Jinzhong, Changzhi, and Jincheng. GWS increases with comparable amplitudes are found in Zhumadian and Xinyang, in the southeastern part of Henan Province. Except
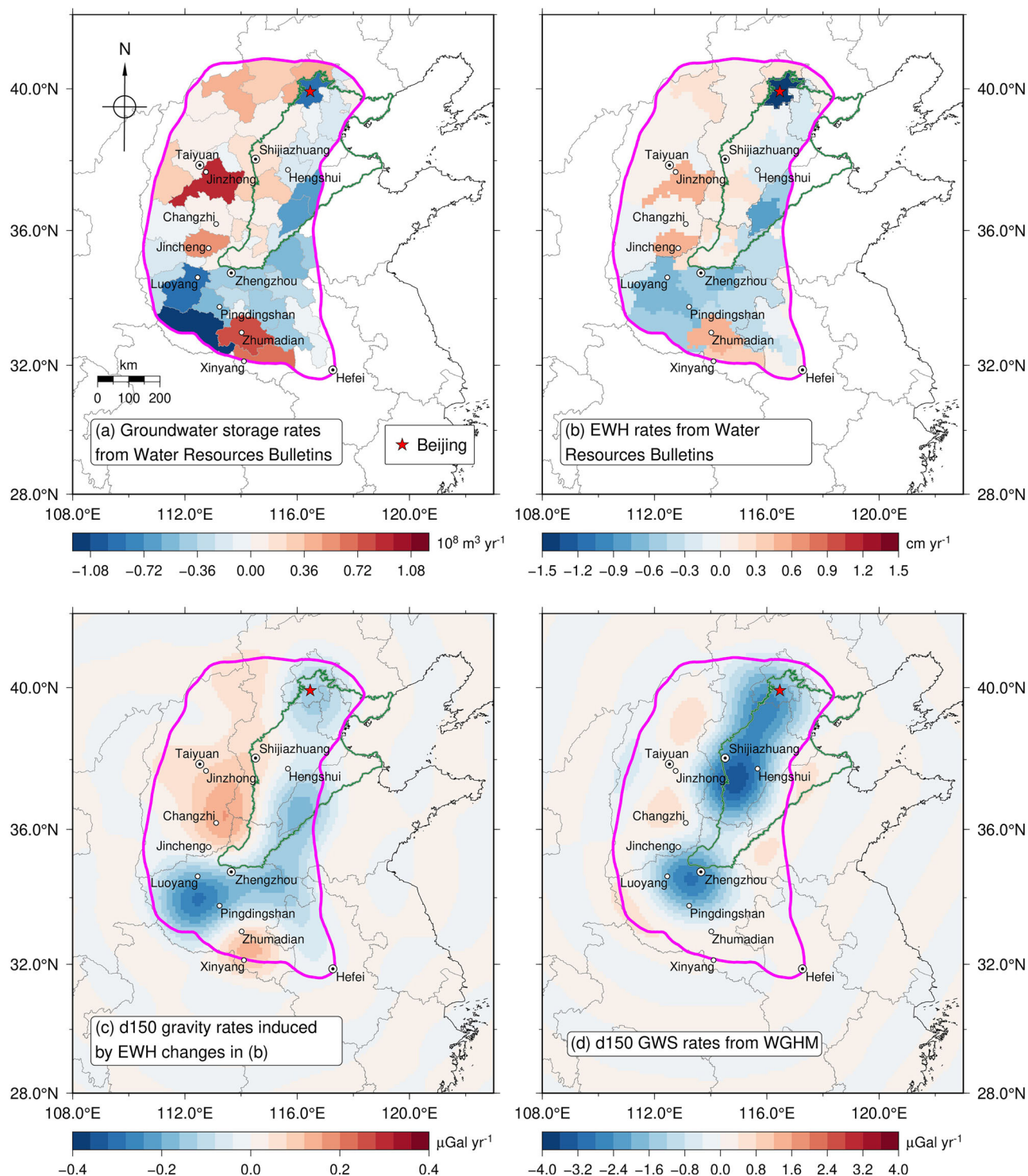
Fig. 6 Water Resources Bulletin– and WGHM-derived d150 gravity rates. a Spatial pattern of shallow groundwater storage (GWS) rates in North China based on the official water resources bulletins from two municipalities (Beijing and Tianjin) and five provinces (Hebei, Henan, Shandong, Shanxi, and Anhui); **b** rates of the equivalent water heights (EWHs) inferred from panel **a**; **c** d150 rates of gravity changes from the equivalent water height changes; and **d** d150 GWS rates from WGHM. The magenta lines denote the boundary of the region of interest, the green lines show the boundary of the NCP, the black lines indicate the land-ocean boundary, and the gray lines show the provincial borders. Note that each panel has an individual color bar.

for the increase in Henan Province, the spatial pattern of the d150 WRB-based GWS rates (Fig. 6c) is in good agreement with the d150 ground-based residual rates (Fig. 5e).

Despite their similar spatial patterns, there are large differences in magnitude between the WRB-based GWS rates (Fig. 6c) and the ground-based residual rates (Fig. 5e). For example, the mean

d150 rate in the NCP induced by groundwater depletion based on the WRB is −0.07 μGal yr^{-1} from 2009 to 2016. Conversely, the mean d150 ground-based residual rate in the NCP is −2.07 μGal yr^{-1} from September 2009 to September 2016. The WRB-based GWS rate accounts for less than 3% of the ground-based residual rate. This discrepancy may be explained by the fact that (1) their

temporal coverages are different. The official bulletins are issued annually; therefore, the WRB-based rates cover a longer period (January 2009–December 2016). Recent studies have revealed a sub-regional recovery of GWS in the NCP after 2015, resulting from the South-to-North Water Diversion Project[15,16]. This recovery has alleviated the GWS depletion in the NCP, resulting in a lower GWS rate from January 2009 to December 2016 than from September 2009 to September 2016; (2) the WRB-based estimate only includes GWS changes in the shallow unconfined aquifers[3,11]. In contrast, the ground-based residuals include GWS changes from both shallow unconfined and deep confined aquifers, as well as gravity changes induced by possible tectonic effects. For example, the ground-based residual rate map highlights a region with an evident gravity increase in Shanxi Province (Fig. 5e). This region is on the Taihangshan sub-block (part of the North China Plain block), where possible upwelling of asthenospheric material has been reported[49]. However, determining the effect of tectonic activities on gravity changes is beyond the scope of the current study; (3) the d150 ground-based residual rate may be subject to large uncertainty. The isolation of GWS depends on the removal of water storages using a hydrological model (WGHM in our case), whose uncertainty is unknown and will propagate into the uncertainty of the residual estimate.

The GWS estimates from WGHM 2.2d in North China were previously reported to be not sensitive to the actual GWS changes[50]. Here, we estimate the d150 gravity rates from the GWS changes provided by WGHM 2.2d. The WGHM GWS changes for the same months as the terrestrial gravity measurements were used. The WGHM-based d150 GWS rates (Fig. 6d) reveal gravity decreases mainly confined to the NCP and the northern part of Henan Province. The mean rate in the NCP is -1.57 µGal yr^{-1}, smaller than that of the d150 ground-based residuals (Fig. 5e). The spatial patterns of the WGHM-based GWS rates differ greatly from those of the d150 residual rates: (1) the decrease in the NCP is more severe in the piedmont regions than in the eastern regions and (2) the center of the decrease in Henan Province is moving northward, and no decrease is found in Anhui Province. Although the d150 ground-based residual rate in Fig. 5e may be subject to large uncertainty, these differences imply that WGHM 2.2d may not fully capture the complete water storage changes in North China.

Acceleration in the gravity increase over the NCP. The mean d150 gravity changes averaged over the NCP show an overall increasing trend during the study period (Supplementary Fig. 13) and highlight an acceleration in the gravity increase from 2012 to 2016. This acceleration started in April 2012 with a rate of 3.52 ± 2.81 µGal yr^{-1} from April 2012 to September 2016, nearly tripling the rate prior to April 2012. From April 2012 through April 2015, the acceleration rate reached 12.76 ± 3.24 µGal yr^{-1}. Zhao et al.[17] reported an acceleration in land subsidence in the NCP during the period of 2013–2016 based on GPS vertical measurements, ranging from ~2 cm yr^{-1} to ~10 cm yr^{-1}. Accordingly, the acceleration in the gravity changes from 2012 to 2016 is likely linked to the accelerated land subsidence. Note that the gravity changes show a decreasing trend from 2015 to 2016. If this decreasing trend continues, the acceleration in the gravity changes will be mitigated.

Gravity increases in Shanxi Province. An increasing pattern is evident in the d150 residual gravity rates in Shanxi Province (Fig. 5d). This pattern was also detected by Feng et al.[50] using the high-resolution Tongji-RegGrace2019 model, which is a regularized GRACE solution up to degree 180[51]. The d150 residual

rates increase from north to south in Shanxi, and the region with the largest gravity increase (approximately 3.6 µGal yr^{-1}) covers the majority of the cities of Changzhi and Jincheng and part of the city of Linfen. The mean d150 time series of the gravity changes within this region (Supplementary Fig. 14a) shows an overall increasing trend, with a large drop occurring in 2012 and a dramatic increase from April 2013 to April 2015. The annual precipitations in Changzhi, Jincheng, and Linfen, according to the Shanxi WRB, show no dramatic changes from 2013 to 2015 (Supplementary Fig. 14b), implying that the gravity increase here is unlikely caused by surplus rainfall. The GWS rates derived from the WRBs are also small (approximately 0.25 µGal yr^{-1}; Fig. 6c) in this region. The region with an evident gravity increase also includes a large reservoir. The Zhangfeng Reservoir is located on the Qinhe River, a tributary of the Yellow River. The total capacity of the Zhangfeng Reservoir is 0.394 km^3, approximately 100 times smaller than that of the Three Gorges Reservoir (~39.3 km^3). The Zhangfeng Reservoir began impoundment in late 2007. The water level reached its maximum operational height of 759 m in October 2017, creating a lake with an area of 14.36 km^2 (http://www.chinawater.com.cn/newscenter/df/sx/201710/t20171020_493200.html). Even though WGHM provides estimations of water storage changes in reservoirs, those for the Zhangfeng Reservoir are not included in the latest WGHM 2.2d (Supplementary Fig. 14c).

Based on the published water level and volume records for the Zhangfeng Reservoir, we derived a quadratic relationship between the reservoir volume and water level (see Supplementary Note 5 for details). Applying a least-squares fitting to the water levels in Table S1, we obtained a water level change rate of 2.86 m yr^{-1} at the Zhangfeng Reservoir from 2009 to 2016. Assuming that the area of the Zhangfeng Reservoir remains the same (14.36 km^2), the mass changes are only associated with the changes in the water level. Note that this assumption leads to overestimating the gravity changes induced by water impoundment. Following this assumption, we converted the water level change rates into gravity rates (Supplementary Fig. 14f). The estimated gravity rates induced by the water impoundment of the Zhangfeng Reservoir are less than 0.10 µGal yr^{-1}, too small to be a substantial contributor to the gravity increase in the southern part of Shanxi Province.

Conclusions

This study aims to provide new information to the scientific community, i.e., the series of high-resolution time-variable gravity field solutions recovered solely from terrestrial gravity measurements (IGP-NorthChina2022TG). One key challenge arises when recovering the gravity field in North China using terrestrial measurements: the recovery of the regional gravity field from the sparsely (and unevenly) distributed and locally available observations. Terrestrial measurements are subject to geographical and environmental constraints, resulting in an uneven distribution of observations. For example, the distribution of observations is dense in the Beijing-Tianjin region, but sparse in Henan Province (Fig. 1b). In this study, we relied on a Slepian localization analysis to recover the regional gravity field in North China from terrestrial gravity measurements. We presented a tailored method for selecting the optimal parameters in the Slepian analysis. The good agreement between the GRACE- and ground-based results up to degree 60 confirmed the robustness and reliability of the proposed method, favoring the combination of these two types of measurements in the future. IGP-NorthChina2022TG also agrees reasonably well with independent in situ absolute gravity measurements.

IGP-NorthChina2022TG provides degree 150 (spatial resolution of ~120 km) time-variable gravity field solutions from

September 2009 to September 2016 on a semi-annual basis. The analysis of the recovery process may provide useful information for refining the gravity network in North China (see Supplementary Note 6 for details). The degree 150 residual gravity rates estimated from IGP-NorthChina2022TG, with the gravity rates induced by vertical displacements removed, show much finer spatial resolution and stronger signal strength compared with GRACE-derived rates for investigations at sub-regional scales. These residual rates may complement GRACE-based analyses of GWS changes and other geophysical processes in North China. The degree 150 gravity time series also provide insights into the time-variable changes, e.g., the acceleration of the gravity increase after April 2012 in the NCP corresponds well with the acceleration of the land subsidence. As the gravity campaign over the network in North China continues and adjustment techniques evolve[31,52], regular refinement and updates of IGP-NorthChina2022TG will be possible.

Methods

Datasets. The core datasets used in this work are 15 repeated survey campaign measurements from a gravity network in North China between September 2009 and September 2016, provided by the Gravity Network Centre of China. Using multiple gravimeters such as Scintrex CG-5, LaCoste-Romberg G, and FG-5, these measurements were carried out roughly on a semi-annual basis, with one campaign around April and the other one around September in each year[32]. After correcting for effects from the earth tide, ocean tide, air pressure, and polar motion, the network adjustment was performed using the pyBACGS program[31,52], a part of the Geoist package (https://github.com/igp-gravity/geoist). The Bayesian adjustment model in pyBACGS allows for an effective estimation of the drift rate and the scale factor for each gravimeter, especially in the case of long-term gravity survey campaigns with multiple gravimeters[53]. The network adjustments for all 15 campaigns yielded an average accuracy of 7.2–9.0 μGal. The locations of the 287 gravity stations covered by all 15 survey campaigns are shown in Fig. 1b. The positions of the most marginal stations generate the boundary (the magenta line in Fig. 1b) of the region of interest.

The auxiliary datasets include the Gravity Recovery and Climate Experiment (GRACE) gravity field solutions and the WaterGAP Global Hydrology Model (WGHM). We collected GRACE level-2 release 06 products from three processing centers: the Center for Space Research at the University of Texas, the GeoForschungsZentrum, and the Jet Propulsion Laboratory. Each level-2 product consists of a set of spherical harmonic (SH) coefficients up to degree and order 60. WGHM simulates water flows and water storage at a global scale. The spatial resolution of the WGHM grid, λ_{WGHM}, is 0.5°. The climate forcing for WGHM includes air temperature, precipitation, downward shortwave radiation, and downward longwave radiation, which are taken from a number of global meteorological datasets[47]. Note that WGHM provides an estimate of the groundwater storage (GWS), as well as storage for nine other compartments (canopy, soil moisture, snow, local lake, global lake, local wetland, global wetland, reservoir, and river).

Model selection. The Slepian approach requires a region Γ, a maximum spherical harmonic expansion degree N, and the number J_{opt} of the Slepian basis functions (Supplementary Methods 2, Supplementary Figs. 1 and 2). The region Γ is the region of interest, which is outlined in Fig. 1b. The limiting factor for the maximum expansion degree N comes from the spatial data gaps[54], which, in our case, reflect the sparse spatial distribution of the gravity measurements. For the truncation level J_{opt}, even

though the Shannon number provides an approximate estimate, an iterative selection procedure is often adopted in practical applications[54–57]. Following the strategies devised by Plattner and Simons[54] and Han et al.[57], we propose a two-step procedure to select the optimal truncation level J_{opt}. The first step covers the strategy to find the number J_{opt} for a given expansion degree n. In the second step, we compare results for a series of expansion degrees n and select the maximum degree N. The strategy of step one is as follows.

(1) Construct synthetic gravity fields based on the model outputs from WGHM 2.2d. First, we retrieved the total water storage (TWS) by summing all the storage from the 10 compartments. We obtained 15 TWS results between September 2009 and September 2016, consistent with the period of the terrestrial gravity measurements. We then converted the TWS into equivalent water heights (EWHs). Next, we expanded these EWHs into SH coefficients f_{nm}. The SH coefficients f_{nm} are up to degree and order 360 (the value 360 equals $180/\lambda_{WGHM}$). Finally, we computed the gravity changes from these SH coefficients as the synthetic gravity fields based on the following relation:[58]

$$\Delta g(\theta, \lambda) = \frac{GM}{a^2} \sum_{n=1}^{N_0} (n-1) \sum_{m=-n}^{n} f_{nm} Y_{nm}(\theta, \lambda) \qquad (1)$$

where (θ, λ) denotes the colatitude and longitude of the point $(0 \le \theta \le \pi$ and $0 \le \lambda < 2\pi)$, $Y_{nm}(\theta, \lambda)$ are the spherical harmonic function of degree n and order m, GM is the product of the gravitational constant and the mass of the Earth, a is the semi-major axis of the Earth, and N_0 denotes different SH expansion degrees ($N_0 = 360, 180, 150, 120, 90,$ and 60). The unit of the derived gravity changes is μGal (1 μGal $= 1 \times 10^{-8}$ m/s^2).

(2) Generate true gravity signals for a given degree N_0 at the repeated survey gravity stations (see Fig. 1b) in the region of interest. After obtaining the synthetic gravity fields from September 2009 to September 2016 for different expansion degrees N_0 in step (1), we removed the mean from each N_0 series. All the tests were conducted using the gravity changes for different N_0 in September 2009. The derived gravity changes for different degrees N_0 in September 2009 are shown in Supplementary Figs. 3b–g. For a given degree N_0, the values at the repeated survey gravity stations linearly interpolated from the corresponding N_0 field are used as the true gravity signals in the following analysis.

(3) Perform the perturbation process for five alternative expansion degrees N_0 (180, 150, 120, 90, and 60). For each degree N_0, we first generated 100 realizations of Gaussian random noise with zero mean and a standard deviation of 3 μGal, the typical noise level for the relative gravity measurements[59]. By adding these noise fields to each true N_0 gravity signal, we created 100 new datasets with perturbations ready for gravity field recovery using the Slepian approach. We recovered the gravity field for each new dataset using the $J = 1, 2, 3, ..., 50$ Slepian basis functions. In total, we completed 5000 recoveries per given spherical harmonic degree N_0. The computation load is extensive, requiring approximately 12 h and 32 h to finish 5000 recoveries for $N_0 = 150$ and $N_0 = 180$, respectively, on a modern desktop computer (Intel i9 2.5 GHz, eight cores processor). Next, we adopted the Bayesian information criterion (BIC) that includes a penalty term increasing with the number of parameters in the model selection process. Given a set of Slepian-recovered model results with different truncation levels J, we have

$$BIC = J \cdot \ln(P) - 2 \ln(L) \qquad (2)$$

where P is the number of observations, and L is the maximum value of the likelihood function. The BICs were first evaluated over the entire region of interest (ROI) for different truncation

Table 1 Different numbers J correspond to the lowest BICs for different degrees N_0 from the perturbed selection process.

Degree N_0	60	90	120	150	180
Number J corresponds to the lowest BIC_{ROI} (evaluated over ROI with all stations)	3	13	18	23	28
Number J corresponds to the lowest BIC_{sparse} (evaluated over a region with sparse stations)	4	13	16	23	17
Number J equals to the Shannon number	3	8	14	22	32

numbers J. This series of BICs is denoted BIC_{ROI}. To highlight the influence of the sparsity of the gravity measurements, we also evaluated the BICs over the southern part of the region of interest, where the gravity stations are sparse (the region outlined by the yellow dashed line in Fig. 1b), resulting in another series of BICs denoted BIC_{sparse}. For each new dataset, we obtained two series of BICs ($J = 1, 2, 3,…,50$). Finally, we averaged the BIC_{ROI} and BIC_{sparse} series from all 100 datasets to obtain two mean BIC series. In these two derived mean BIC series, the truncation number J corresponding to the lowest BIC value is J_{opt}. The mean BIC_{ROI} and BIC_{sparse} series for $N_0 = 150$ are shown in Supplementary Fig. 4a. Both series first decrease to the lowest value and then gradually increase. The optimal truncation level J_{opt} selected by the perturbation process was 23 for $N_0 = 150$. For $N_0 = 180, 120, 90$, and 60, the mean BIC_{ROI} and BIC_{sparse} series exhibit similar patterns as the degree 150 series (Supplementary Fig. 5). Different numbers J correspond to the lowest BICs for different degrees N_0 are listed in Table 1.

At the completion of the first step, we found the optimal truncation levels J_{opt} for the different degrees N_0. In the second step, we focused on the selection of the maximum SH expansion degree based on the behavior of the BIC_{ROI} and BIC_{sparse} series. As shown in Table 1 and Supplementary Fig. 5, the numbers J corresponding to the lowest value for the BIC_{ROI} series and the values for the BIC_{sparse} series are very close to each other or identical for $N_0 = 60, 90, 120$, and 150. For $N_0 = 180$, there is a big discrepancy between these two values of J (28 and 17). Therefore, the maximum expansion degree N was selected to be the one with the highest maximum SH degree N_0 for which the numbers J_{opt} determined by the BIC_{ROI} and BIC_{sparse} series were consistent. In our case, the maximum SH expansion degree N was chosen to be 150.

For the maximum degree $N = 150$ (d150), using the true gravity signals at the repeated survey gravity stations (Supplementary Fig. 6a) and $J_{opt} = 23$, the recovered d150 gravity field, g_{model}^{d150}, is shown in Supplementary Fig. 6b. The residual between g_{model}^{d150} and the original d150 field, g_{true}^{d150} (Supplementary Fig. 3d), is shown in Supplementary Fig. 6c. The correlation coefficient between g_{model}^{d150} and g_{true}^{d150} is 0.984. We also computed the variance reduction (VR; see Han et al.[60] and Rahimi et al.[61]): $VR = [1 - var(g_{true}^{d150} - g_{model}^{d150})/var(g_{true}^{d150})] \times 100\%$, where var() is an operator calculating the variance. The derived g_{model}^{d150} agrees with g_{true}^{d150}, yielding a VR of more than 96.7%. These good agreements between g_{model}^{d150} and g_{true}^{d150} imply that the gravity field recoveries using $J_{opt} = 23$ and the d150 true gravity signals are sufficiently accurate in the region of interest.

Broadband leakage mitigation. At this point, we have finished recovering the degree N_0 gravity fields using the synthetic degree N_0 gravity signals at the repeated stations. However, the gravity signals at the Earth's surface, i.e., the terrestrial gravity observations, contain the spectrum up to an infinite degree ($N_0 = \infty$). The difference between the given recovery degree (N_0) and that contained in the input signals leads to an issue called broadband leakage, which can be described as follows: when recovering a degree N_0 field, the high degree ($>N_0$) components in the input signal will affect the estimation of the low degree ($\leq N_0$) coefficients. This broadband leakage issue has been reported in previous studies[34,55,57,62]. However, few studies have addressed the mitigation of broadband leakage[57].

We implemented an iterative strategy based on the work of Han et al.[57] to mitigate broadband leakage. First, the gravity signals of degree 360 (d360) at the repeated survey gravity stations were generated to represent the real terrestrial gravity measurements (Supplementary Fig. 6d) based on the d360 gravity changes from WGHM (Supplementary Fig. 3b). Note that degree 360 is the maximum degree for gravity changes that we can obtain from the WGHM outputs (spatial resolution of 0.5°). Next, we recovered the d150 gravity field using these d360 measurements. The recovered d150 field is shown in Supplementary Fig. 6e, while the residual between the recovered and original d150 fields is shown in Supplementary Fig. 6f. The recovered d150 field using the d360 measurements (Supplementary Fig. 6e) differs notably from the result recovered using the d150 measurements (Supplementary Fig. 6b) in both spatial pattern and strength, especially in the regions around Beijing, Taiyuan-Shijiazhuang-Hengshui, and Zhengzhou. Large discrepancies are also evident in Supplementary Figs. 6c and 6f. The large discrepancies between Supplementary Figs. 6e and 6b, as well as 6c and 6f highlight the existence and effects of broadband leakage.

Next, we removed the high-degree components from the d360 measurements using the Gaussian spatial averaging approach. Assuming that $\bar{g}_j$ are the Gaussian-weighted average values, we have[63]

$$\bar{g}_j = \frac{\sum_{i=1}^{k} g_i \cdot W(\psi_i)}{\sum_{i=1}^{k} W(\psi_i)}$$

$$W(\psi) = \frac{2be^{-b(1-\cos\psi)}}{1 - e^{-2b}} \qquad (3)$$

$$b = \frac{\ln 2}{(1 - \cos(r/R))}$$

where r is the averaging radius, ψ_i is the spherical distance between the points g_i and g_j ($0 \leq \psi_i \leq \pi$), $W(\psi)$ are the Gaussian averaging functions, g_i ($i = 1, ..., k$) are the gravity measurements falling in the averaging radius, R is the Earth's mean radius (6371 km), and b is a dimensionless parameter.

To mitigate the effects caused by the broadband leakage, removing the high degree ($>N_0$) components from the d360 measurements, as much as possible, is necessary. An iterative process achieves this.

(1) For the averaging radius r, an initial value of 80 km is set. Then, the Gaussian-weighted average $\bar{g}$ is derived according to Eq. 3.
(2) The d150 gravity field is recovered based on $\bar{g}$, and the result is denoted $g_{model}^{(i)}$, where i indicates the iteration number.
(3) The root mean square (RMS) difference between $g_{model}^{(i)}$ and the original field g_{true}^{d150} is calculated.
(4) The next iteration begins by increasing the averaging radius r by 1 km.

The RMS difference reaches the smallest value when r equals 99 km (after 20 iterations). After the 99-km Gaussian spatial averaging is applied to the d360 measurements, the derived $\bar{g}$ values (Supplementary Fig. 6g) are consistent with the d150 measurements (Supplementary Fig. 6a). We then recovered the d150 gravity field again. The final d150 field is shown in
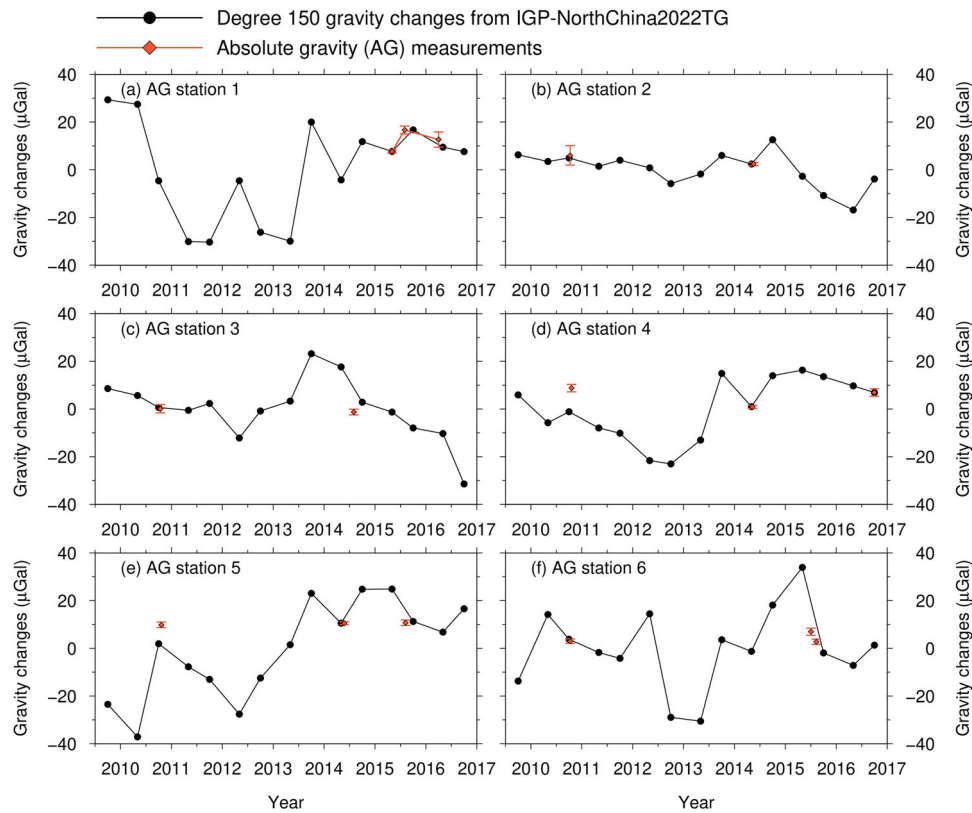
Fig. 7 Gravity variations at the gravity stations derived from degree 150 IGP-NorthChina2022TG and in situ absolute gravity (AG) measurements. Comparisons at **a** station 1; **b** station 2; **c** station 3; **d** station 4; **e** station 5; and **f** station 6. The locations of these stations are denoted by yellow crosses in Fig. 5a. Our gravity field recovery procedure does not include these in situ AG measurements. The red error bars indicate the accuracy of absolute gravity measurements. Offsets are added to the AG-derived results compared with the degree 150 estimates.

Supplementary Fig. 6h, while the residual between the recovered and original d150 fields is shown in Supplementary Fig. 6i. The recovered d150 field using the d360 measurements after the Gaussian spatial average agrees well with the result recovered using the d150 measurements (Supplementary Fig. 6b), suggesting that the broadband leakage has effectively been mitigated. Despite the limitation of using the d360 synthetic gravity changes to represent the real time variable gravity measurement, the strategy proposed here represents a major advance in mitigating broadband leakage in Slepian analyses.

Comparison of degree 150 gravity time series and independent absolute gravity measurements. To assess the derived d150 gravity field solutions, we compared the d150 gravity changes with in situ absolute gravity (AG) measurements at six gravity stations in the region of interest. The locations of these stations are shown in Fig. 5a. The AG measurements at station 1 were collected by our group using FG5X-249 and A10-034 gravimeters. The AG measurements were made with FG5/5X and A10 gravimeters for the rest of the stations and were provided by the National Earthquake Data Center (http://data.earthquake.cn). In general, no less than 25 h of repeated measurements were collected at each station, with 25 and 50 accepted sets for the FG5/5X and A10 gravimeters in each measurement. Each set includes 100 free-fall drops. The final gravity values were transferred from the instrumental height to the ground. The accuracy of these AG measurements ranges from 0.60 μGal to 4.09 μGal. None of the AG measurements were included in our d150 gravity field recovery procedure or the previous network adjustment procedure.

In general, the d150 gravity changes at the six stations corresponded well with the in situ AG measurements (Fig. 7).

Large discrepancies (approximately 10 μGal) were found in 2010 at stations 4 and 5 (Fig. 7d, e). Because of the limited and sparse in situ AG measurements, the assessment shown here may be subject to large uncertainties. Moreover, the spatial resolutions and spectral coverage differ between the AG measurements and the d150 gravity changes. (1) The AG measurements at a single station primarily represent local mass changes within a limited area and depend on the local hydrogeological characteristics. In contrast, the d150 gravity changes reflect mass changes within an area determined by the spatial resolution of the degree 150 fields (180°/150 = 1.2° in half-wavelength). (2) The AG measurements contain the spectrum up to an infinite degree, while the d150 gravity changes are truncated at degree 150. These spatial resolutions and spectral coverage differences may result in the mismatch between the AG measurements and the d150 time series in 2010 at stations 4 and 5. The assessment shows that the gravity changes from our d150 fields agree reasonably well with the in situ AG measurements. A thorough assessment of IGP-NorthChina2022TG, however, requires terrestrial gravity measurements at additional stations with longer temporal coverages.

Gravity changes from GRACE. During the period of the terrestrial gravity measurements, the September 2016 GRACE data were missing. We used the August 2016 GRACE data instead. As a common postprocessing practice, we replaced the degree-two order-zero coefficients with the more reliable estimates from satellite laser ranging[64] and added back the degree-one coefficients[65]. After the above corrections, the gravity changes were computed using Slepian functions from the SH coefficients[66,67], with the truncation number $J_{opt} = 3$ (same as the d60 terrestrial case). When estimating mass changes using GRACE

SH coefficients, a filtering procedure is often necessary to suppress the errors in these coefficients. However, the Slepian method can extract information from GRACE data without further filtering or smoothing[66,67]. Next, we estimated the rates of the gravity changes derived using the Slepian functions. We adopted an ensemble mean of the rates from the three data centers to reduce the uncertainties in the GRACE data[68]. Because the ensemble GRACE rates were derived using Slepian functions (Fig. 2d), we also obtained ensemble GRACE rates using two popular DDK[69] and Gaussian smoothing[70] filters. The ensemble rates derived using DDK5 and 200-km Gaussian smoothing are shown in Figs. 2e and 2f, respectively. Other DDK and Gaussian smoothing alternatives yielded similar spatial patterns in the region of interest (see Supplementary Note 3, Supplementary Figs. 10 and 11).

Gravity effects induced by vertical displacements. Based on the GPS-derived vertical displacements in North China, we accounted for the gravity effects induced by vertical displacements using the following relation:[39,71]

$$\frac{dg_{res}^{degree}}{dt} = \frac{dg_{TG}^{degree}}{dt} - \gamma_g \frac{dh_{GPS}^{degree}}{dt} \tag{4}$$

where TG stands for terrestrial gravity, degree indicates the maximum expansion degree (d60 or d150), res indicates the residual term, and γ_g is the vertical gravity gradient. We compared three gravity gradients in North China, namely the free-air gradient ($\gamma_g = -3.086$ µGal cm^{-1}), the Bouguer gradient ($\gamma_g = -1.967$ µGal cm^{-1}), and the Bouguer-corrected free-air gradient of a spherical body (BCFAG$_{spherical}$). Compared to the free-air and Bouguer gradients, the BCFAG$_{spherical}$ is more realistic in volcanic context and thus widely adopted to address gravity changes of a magma reservoir modeled as a spherical body[33,40,41]. Taking into consideration the mass accompanying the deformation, the BCFAG$_{spherical}$ depicts the changes in gravity that result from an elevation change[40,41]

$$\gamma_g = \text{free-air gradient} + \frac{4\pi G \rho_0}{3} \times 10^6 \text{ µGal cm}^{-1} \tag{5}$$

where G is the gravitational constant (6.674×10^{-11} N m^2 kg^{-2}) and ρ_0 is the density of the source in units of kg m^{-3}.

Since the land subsidence in the NCP has a strong relationship with groundwater overexploitation[5], we assume a spherical body of groundwater by analogy with the volcanic case when applying the BCFAG$_{spherical}$ correction. The BCFAG$_{spherical}$ results in $\gamma_g = -2.806$ µGal cm^{-1} with groundwater density $\rho_0 = 1000$ kg m^{-3}.

References

1. Tapley, B. D. et al. Contributions of GRACE to understanding climate change. *Nat. Clim. Chang.* **5**, 358–369 (2019).
2. Liu, C., Yu, J. & Eloise, K. Groundwater exploitation and its impact on the environment in the North China plain. *Water Int.* **26**, 265–272 (2001).
3. Feng, W., Shum, C., Zhong, M. & Pan, Y. Groundwater storage changes in china from satellite gravity: an overview. *Remote Sens.* **10**, 674 (2018).
4. Xia, J., Zhang, L., Liu, C. & Yu, J. Towards better water security in North China. *Water Resour. Manage.* **21**, 233–247 (2007).
5. Guo, H. et al. Groundwater-derived land subsidence in the North China Plain. *Environ. Earth Sci.* **74**, 1415–1427 (2015).
6. Su, G. et al. Spatiotemporal evolution characteristics of land subsidence caused by groundwater depletion in the North China plain during the past six decades. *J. Hydrol.* **600**, 126678 (2021).
7. Pang, Y. et al. The modulation of groundwater exploitation on crustal stress in the North China Plain, and its implications on seismicity. *J. Asian Earth Sci.* **189**, 104141 (2020).
8. Wang, D. et al. Determination of tectonic and nontectonic vertical motion rates of the North China Craton using dense GPS and GRACE data. *J. Asian Earth Sci.* **236**, 105314 (2022).
9. Zhong, M. et al. Trend of China land water storage redistribution at medi- and large-spatial scales in recent five years by satellite gravity observations. *Sci. Bull.* **54**, 816–821 (2008).
10. Su, X., Ping, J. & Ye, Q. Terrestrial water variations in the North China Plain revealed by the GRACE mission. *Sci. China Earth Sci.* **54**, 1965–1970 (2011).
11. Feng, W. et al. Evaluation of groundwater depletion in North China using the Gravity Recovery and Climate Experiment (GRACE) data and ground-based measurements. *Water Resour. Res.* **49**, 2110–2118 (2013).
12. Huang, Z. et al. Subregional-scale groundwater depletion detected by GRACE for both shallow and deep aquifers in North China Plain. *Geophys. Res. Lett.* **42**, 1791–1799 (2015).
13. Gong, H. et al. Long-term groundwater storage changes and land subsidence development in the North China Plain (1971–2015). *Hydrogeol. J.* **26**, 1417–1427 (2018).
14. Pan, Y. et al. Detection of human-induced evapotranspiration using GRACE satellite observations in the Haihe River basin of China. *Geophys. Res. Lett.* **44**, 190–199 (2017).
15. Long, D. et al. South-to-north water diversion stabilizing Beijing's groundwater levels. *Nat. Commun.* **11**, 3665 (2020).
16. Zhang, C. et al. Sub-regional groundwater storage recovery in North China Plain after the South-to-North water diversion project. *J. Hydrol.* **597**, 126156 (2021).
17. Zhao, Q. et al. Geodetic and hydrological measurements reveal the recent acceleration of groundwater depletion in North China Plain. *J. Hydrol.* **575**, 1065–1072 (2019).
18. Liu, R., Li, J., Fok, H. S., Shum, C. K. & Li, Z. Earth surface deformation in the North China Plain detected by joint analysis of GRACE and GPS data. *Sensors* **14**, 19861–19876 (2014).
19. Chen, J. L. et al. Applications and challenges of GRACE and GRACE follow-on satellite gravimetry. *Surv. Geophys.* **43**, 305–345 (2022).
20. Swenson, S. & Wahr, J. Post-processing removal of correlated errors in GRACE data. *Geophys. Res. Lett.* **33**, L08402 (2006).
21. Chen, J. L., Wilson, C. R., Tapley, B. D. & Grand, S. GRACE detects coseismic and postseismic deformation from the Sumatra-Andaman earthquake. *Geophys. Res. Lett.* **34**, L13302 (2007).
22. Chen, J. L., Wilson, C. R., Tapley, B. D., Save, H. & Cretaux, J. F. Long-term and seasonal Caspian Sea level change from satellite gravity and altimeter measurements. *J. Geophys. Res.: Solid Earth* **122**, 2274–2290 (2017).
23. Tangdamrongsub, N., Hwang, C., Shum, C. K. & Wang, L. Regional surface mass anomalies from GRACE KBR measurements: Application of L-curve regularization and a priori hydrological knowledge. *J. Geophys. Res.: Solid Earth* **117**, B11406 (2012).
24. Save, H., Bettadpur, S. & Tapley, B. D. High-resolution CSR GRACE RL05 mascons. *J. Geophys. Res.: Solid Earth* **121**, 7547–7569 (2016).
25. Watkins, M. M., Wiese, D. N., Yuan, D.-N., Boening, C. & Landerer, F. W. Improved methods for observing Earth's time variable mass distribution with GRACE using spherical cap mascons. *J. Geophys. Res.: Solid Earth* **120**, 2648–2671 (2015).

26. Scanlon, B. R. et al. Global evaluation of new GRACE mascon products for hydrologic applications. *Water Resour. Res.* **52**, 9412–9429 (2016).

27. Loomis, B. D., Luthcke, S. B. & Sabaka, T. J. Regularization and error characterization of GRACE mascons. *J. Geod.* **93**, 1381–1398 (2019).

28. Sakumura, C., Bettadpur, S., Save, H. & McCullough, C. High-frequency terrestrial water storage signal capture via a regularized sliding window mascon product from GRACE. *J. Geophys. Res.: Solid Earth* **121**, 4014–4030 (2016).

29. Tregoning, P. et al. ANU GRACE Data Analysis: Characteristics and Benefits of Using Irregularly Shaped Mascons. *J. Geophys. Res.: Solid Earth* **127**, e2021JB022412 (2022).

30. Zhu, Y., Zhan, F. B., Zhou, J., Liang, W. & Xu, Y. Gravity measurements and their variations before the 2008 Wenchuan Earthquake. *Bull. Seismol. Soc. Am.* **100**, 2815–2824 (2010).

31. Chen, S., Zhuang, J., Li, X., Lu, H. & Xu, W. Bayesian approach for network adjustment for gravity survey campaign: methodology and model test. *J. Geod.* **93**, 681–700 (2019).

32. Zhu, Y., Liu, F., Zhang, G. & Xu, Y. Development and prospect of mobile gravity monitoring and earthquake forecasting in recent ten years in China. *Geod. Geodyn.* **10**, 485–491 (2019).

33. Van Camp, M. et al. Geophysics from terrestrial time-variable gravity measurements. *Rev. Geophys.* **55**, 938–992 (2017).

34. Simons, F. J. & Dahlen, F. A. Spherical Slepian functions and the polar gap in geodesy. *Geophys. J. Int.* **166**, 1039–1061 (2006).

35. Simons, F. J., Dahlen, F. A. & Wieczorek, M. A. Spatiospectral concentration on a sphere. *SIAM Rev.* **48**, 504–536 (2006).

36. Simons, F. J. Slepian functions and their use in signal estimation and spectral analysis. In: *Handbook of Geomathematics. Springer* (eds Freeden W., Nashed M. Z., Sonar T.) (2010).

37. Sun, W., Okubo, S., Fu, G. & Araya, A. General formulations of global co-seismic deformations caused by an arbitrary dislocation in a spherically symmetric earth model-applicable to deformed earth surface and space-fixed point. *Geophys. J. Int.* **177**, 817–833 (2009).

38. Li, J., Chen, J. L. & Wilson, C. R. Topographic effects on coseismic gravity change for the 2011 Tohoku-Oki earthquake and comparison with GRACE. *J. Geophys. Res.: Solid Earth* **121**, 5509–5537 (2016).

39. Müller, J., Naeimi, M., Gitlein, O., Timmen, L. & Denker, H. A land uplift model in Fennoscandia combining GRACE and absolute gravimetry data. *Phys. Chem. Earth Parts A/B/C* **53-54**, 54–60 (2012).

40. Rymer, H. Microgravity change as a precursor to volcanic activity. *J. Volcanol. Geotherm. Res.* **61**, 311–328 (1994).

41. Dzurisin, D. et al. Geophysical observations of Kilauea Volcano, Hawaii, 2. Constraints on the magma supply during November 1975–September 1977. *J. Volcanol. Geotherm. Res.* **7**, 241–269 (1980).

42. Shen, C., Xuan, S., Zou, Z. & Wu, G. Trends in gravity changes from 2009 to 2013 derived from ground-based gravimetry and GRACE data in North China. *Geod. Geodyn.* **6**, 423–428 (2015).

43. Hao, H. et al. Terrestrial water storage variation in Hebei plain area of China, based on ground surface gravimetry. *Geod. Geodyn.* **12**, 190–196 (2021).

44. Hwang, C. et al. Time-varying land subsidence detected by radar altimetry: California, Taiwan and north China. *Sci. Rep.* **6**, 28160 (2016).

45. Yu, W., Gong, H., Chen, B., Zhou, C. & Zhang, Q. Combined GRACE and MT-InSAR to assess the relationship between groundwater storage change and land subsidence in the Beijing-Tianjin-Hebei Region. *Remote Sens.* **13**, 3773 (2021).

46. Müller Schmied, H. et al. The global water resources and use model WaterGAP v2.2d - Standard model output. PANGAEA (2020).

47. Müller Schmied, H. et al. The global water resources and use model WaterGAP v2.2d: model description and evaluation. *Geosci. Model Dev.* **14**, 1037–1079 (2021).

48. Chen, J., Famiglietti, J. S., Scanlon, B. R. & Rodell, M. Groundwater storage changes: present status from GRACE observations. *Surv. Geophys.* **37**, 397–417 (2016).

49. Shi, Y., Liao, X., Zhang, D., Liu, C. & Wan, F. Influence of asthenosphere material movement on the movement characteristics of fault basins surrounding the Ordos block (in Chinese). *Chin. J. Geophys.* **60**, 2614–2627 (2017).

50. Feng, T., Shen, Y., Chen, Q., Wang, F. & Zhang, X. Groundwater storage change and driving factor analysis in north China using independent component decomposition. *J. Hydrol.* **609**, 127708 (2022).

51. Chen, Q. et al. High-resolution GRACE monthly spherical harmonic solutions. *J. Geophys. Res.: Solid Earth* **126**, e2019JB018892 (2020).

52. Wang, L., Chen, S., Zhuang, J. & Xu, W. Simultaneous calibration of instrument scale factor and drift rate in network adjustment for continental-scale gravity survey campaign. *Geophys. J. Int.* **228**, 1541–1555 (2022).

53. Chen, Z. et al. Uncertainty Quantification and Field Source Inversion for the Continental-Scale Time-Varying Gravity Dataset: A Case Study in SE Tibet, China. *Pure Appl. Geophys.* **180**, 683–702 (2022).

54. Plattner, A. & Simons, F. J. High-resolution local magnetic field models for the Martian South Pole from Mars Global Surveyor data. *J. Geophys. Res.: Planets* **120**, 1543–1566 (2015).

55. Slobbe, D. C., Simons, F. J. & Klees, R. The spherical Slepian basis as a means to obtain spectral consistency between mean sea level and the geoid. *J. Geod.* **86**, 609–628 (2012).

56. Plattner, A. & Simons, F. J. Internal and external potential-field estimation from regional vector data at varying satellite altitude. *Geophys. J. Int.* **211**, 207–238 (2017).

57. Han, J., Chen, S., Lu, H. & Xu, W. Time-variable gravity field determination using Slepian functions and terrestrial measurements: A case study in North China with data from 2011 to 2013 (in Chinese). *Chin. J. Geophys.* **64**, 1542–1557 (2021).

58. Chao, B. F. & Liau, J. R. Gravity changes due to large earthquakes detected in GRACE satellite data via empirical orthogonal function analysis. *J. Geophys. Res.: Solid Earth* **124**, 3024–3035 (2019).

59. Kennedy, J. R. & Ferré, T. P. A. Accounting for time- and space-varying changes in the gravity field to improve the network adjustment of relative-gravity data. *Geophys. J. Int.* **204**, 892–906 (2016).

60. Han, S.-C., Sauber, J. & Riva, R. Contribution of satellite gravimetry to understanding seismic source processes of the 2011 Tohoku-Oki earthquake. *Geophys. Res. Lett.* **38**, L24312 (2011).

61. Rahimi, A., Li, J., Raoofian Naeeni, M., Shahrisvand, M. & Fatolazadeh, F. On the extraction of co-seismic signal for the Kuril Island earthquakes using GRACE observations. *Geophys. J. Int.* **215**, 346–362 (2018).

62. Plattner, A. & Simons, F. J. Potential-field estimation using scalar and vector slepian functions at satellite altitude. In: *Handbook of Geomathematics* (eds Freeden W., Nashed M., Sonar T.) (2013).

63. Bomfim, E. P., Braitenberg, C. & Molina, E. C. Mutual evaluation of global gravity models (EGM2008 and GOCE) and terrestrial data in Amazon Basin, Brazil. *Geophys. J. Int.* **195**, 870–882 (2013).

64. Loomis, B. D., Rachlin, K. E. & Luthcke, S. B. Improved earth oblateness rate reveals increased ice sheet losses and mass-driven sea level rise. *Geophys. Res. Lett.* **46**, 6910–6917 (2019).

65. Sun, Y., Riva, R. & Ditmar, P. Optimizing estimates of annual variations and trends in geocenter motion and J2 from a combination of GRACE data and geophysical models. *J. Geophys. Res.: Solid Earth* **121**, 8352–8370 (2016).

66. Harig, C. & Simons, F. J. Mapping Greenland's mass loss in space and time. *Proc. Natl. Acad. Sci. USA.* **109**, 19934–19937 (2012).

67. Harig, C. & Simons, F. J. Accelerated West Antarctic ice mass loss continues to outpace East Antarctic gains. *Earth Planet. Sci. Lett.* **415**, 134–141 (2015).

68. Sakumura, C., Bettadpur, S. & Bruinsma, S. Ensemble prediction and intercomparison analysis of GRACE time-variable gravity field models. *Geophys. Res. Lett.* **41**, 1389–1397 (2014).

69. Kusche, J. Approximate decorrelation and non-isotropic smoothing of time-variable GRACE-type gravity field models. *J. Geod.* **81**, 733–749 (2007).

70. Wahr, J., Molenaar, M. & Bryan, F. Time variability of the Earth's gravity field: Hydrological and oceanic effects and their possible detection using GRACE. *J. Geophys. Res.: Solid Earth* **103**, 30205–30229 (1998).

71. Steffen, H., Wu, P. & Wang, H. Optimal locations for absolute gravity measurements and sensitivity of GRACE observations for constraining glacial isostatic adjustment on the northern hemisphere. *Geophys. J. Int.* **190**, 1483–1494 (2012).

72. Han, J. The datasets used in Figs. 1–7 [Data set]. *Zenodo*, https://doi.org/10.5281/zenodo.10403685 (2023).

73. Han, J. The datasets used in the Supplementary Information [Data set]. *Zenodo*, https://doi.org/10.5281/zenodo.10410209 (2023).

74. Wessel, P. et al. The Generic Mapping Tools Version 6. *Geochem. Geophys. Geosyst.* **20**, 5556–5564 (2019).

75. Zhang, P. et al. Active tectonic blocks and strong earthquakes in the continent of China. *Sci. China Ser. D: Earth Sci.* **46**, 13–24 (2003).

76. Deng, Q. et al. Active tectonics and earthquake activities in China (in Chinese). *Earth Sci. Front.* **10**, 66–73 (2003).

77. Tozer, B. et al. Global Bathymetry and Topography at 15 Arc Sec: SRTM15. *Earth Space Sci.* **6**, 1847–1864 (2019).

78. Han, Z., Xu, J., Ran, Y., Chen, L. & Yang, X. Active blocks and strong seismic activity in North China region. *Sci. China Ser. D: Earth Sci.* **46**, 153–167 (2003).

Acknowledgements

Author contributions

J.H. and S.C. conceived and designed the study. H.L., L.J., L.W., and W.X. processed the gravity campaign measurements. J.H. performed the gravity field modeling, analyzed the results, and drafted the paper. S.C. supervised the modeling procedure. S.C., H.Z., and H.S. revised the paper. All authors contributed to the discussion and interpretation of results.

Competing interests

The authors declare no competing interests.

Additional information

Supplementary information The online version contains supplementary material available at https://doi.org/10.1038/s43247-024-01209-w.

Correspondence and requests for materials should be addressed to Shi Chen.

Peer review information *Communications Earth & Environment* thanks the anonymous reviewers for their contribution to the peer review of this work. Primary Handling Editors: Teng Wang, Joe Aslin and Aliénor Lavergne. A peer review file is available.

Reprints and permission information is available at http://www.nature.com/reprints